Non-Chained, Non-Interacting, Stable Single-Domain Magnetite Octahedra in Deep-Sea Red Clay: A New Type of Magnetofossil?

メタデータ	言語: eng
	出版者:
	公開日: 2022-09-01
	キーワード (Ja):
	キーワード (En):
	作成者:
	メールアドレス:
	所属:
URL	https://doi.org/10.24517/00067007

Geochemistry, Geophysics, Geosystems

Key Points:
- We identified five magnetic components in sediment from Ocean Drilling Program Site 777 (the northern Mariana Basin)
- Magnetic and microscopy data revealed that non-chained biogenic magnetite carries a component with low coercivity (<10 mT)
- Non-chained magnetofossils may have been overlooked in geological records

Supporting Information:
Supporting Information may be found in the online version of this article.

Correspondence to:
Y. Usui,
yoichi@jamstec.go.jp

Non-Chained, Non-Interacting, Stable Single-Domain Magnetite Octahedra in Deep-Sea Red Clay: A New Type of Magnetofossil?

Yoichi Usui[1] and **Toshitsugu Yamazaki[2]**

[1]Volcanoes and Earth's Interior Research Center, Research Institute of Marine Geodynamics, Japan Agency for Marine-Earth Science and Technology (JAMSTEC), Yokosuka, Kanagawa, Japan, [2]Atmosphere and Ocean Research Institute, The University of Tokyo, Kashiwa, Chiba, Japan

Abstract Magnetic detection and classification of magnetofossils have been proposed as potential tools for paleoenvironmental studies. Magnetosomes in bacterial species living in different environmental conditions exhibit different grain morphologies and chain configurations, which determine their magnetic properties. Recently, abundant magnetofossils have been reported from unfossiliferous pelagic red clay. However, little is known about their geometry and magnetic properties. Here we report very low coercivity biogenic magnetite in red clay from Ocean Drilling Program (ODP) Site 777 in the northern Mariana Basin. Analyzed sediment showed non-interacting, stable single-domain-like magnetic behaviors. Acquisition of isothermal remanence was decomposed into five components, and a component with mean coercivity below 10 mT accounted for around 25 % of the remanence in some samples. Based on comparisons with semi-quantitative transmission electron microscopy observations of magnetic extracts, this component appears to be carried by octahedral grains with size and shape very similar to biogenic magnetite in red clay from other sites. Micromagnetic calculations indicated that isolated maghemite octahedra may be responsible for the observed low coercivity component. Based on these results, we conclude that the low coercivity component represents non-chained biogenic magnetite that has been oxidized to maghemite. The crystal morphology, geological setting, and lithology do not suggest unusual environmental conditions for ODP Site 777, so the relative amount of chained versus non-chained grains may represent subtle environmental differences. We suggest that non-chained magnetofossils may be widespread in deep-sea sediments. Some methods could overlook the presence of non-chained magnetite, affecting the identification and quantification of magnetofossils.

Plain Language Summary A group of bacteria called "magnetic bacteria" produce chains of magnetite crystals inside their cells. Magnetic bacteria navigate along the geomagnetic field using these magnetite crystals. Magnetic bacteria have been found in a variety of environments in lake and marine sediments. Recently, bacterial magnetite has also been found to be abundant in deep-sea sediment, where supply of organic matter is very low. However, we do not know what kind of magnetic bacteria produces the magnetite in such an environment. To investigate the diversity of the deep-sea bacterial magnetite, we analyzed sediment from the northern Mariana basin using magnetic measurements, microscopic observations, and computer simulations. We found that non-chained bacterial magnetite account for tens of percent of magnetite in the sediment. Although magnetic bacteria that produce non-chained magnetite are known, this is the first time such magnetite has been found in natural sediment in a large quantity. Our results indicate that in the deep-sea there is a greater diversity of magnetic bacteria than previously thought.

1. Introduction

Magnetofossils, fossils of bacterial magnetosomes preserved in sediments and sedimentary rocks, are potential environmental proxies. Their widespread occurrence and ferromagnetism offer particular advantages. Magnetic bacteria and magnetofossils have been found in environments where few other fossils exist (Lefèvre et al., 2010, 2011; Yamazaki & Shimono, 2013), including controversial "fossils" in a Martian meteorite (McKay et al., 1996; Thomas-Keprta et al., 2000, 2001). Magnetosomes typically contain chain(s) of biogenic magnetite or greigite (e.g., Bazylinski & Frankel, 2003; Uebe & Schüler, 2016), although some species

produce non-chained intracellular grains (Li, Menguy, et al., 2020; Liu et al., 2021). Empirically, different species produce different grain morphologies and chain configurations (e.g., Lefèvre & Bazylinski, 2013; Li, Menguy, et al., 2020), so they may be paleoenvironmental indicators. Magnetofossils can be characterized quantitatively in bulk samples by magnetic methods. A single magnetofossil chain behaves similarly to a non-interacting stable single-domain (SSD) magnetic grain (e.g., Dunin-Borkowski et al., 1998; Moskowitz et al., 1993). This characteristic helps distinguish magnetofossils from detrital and diagenetic magnetic particles (e.g., Egli et al., 2010; Kopp & Kirschvink, 2008). Moreover, the effective magnetic anisotropy of magnetosomes depends on the grain morphology and chain configuration (length, grain spacing, crystallographic orientations, etc.). Magnetic anisotropy controls bulk magnetic properties such as coercivity. Magnetic methods complement direct microscopic observations where the chain configuration is difficult to resolve. In particular, recent advances in micromagnetic calculations provide means to simulate the magnetic behaviors of chains using grain morphologies obtained by microscopy (Chang et al., 2018; Gandia et al., 2020; Harrison & Lascu, 2014).

Magnetofossils from different (paleo) environments exhibit different grain morphologies and magnetic properties. Several studies have indicated that more isotropic biogenic magnetite dominates under less reducing conditions (Chang et al., 2018; He & Pan, 2020; Hesse, 1994; Yamazaki & Kawahata, 1998). This observation is consistent with the spatial distribution of magnetic bacteria in surface sediments, where bacteria producing teardrop-shaped magnetite have been found near the oxic-anoxic transition zone (Yamazaki et al., 2019). On the other hand, in a contourite drift, more isotropic magnetofossils were observed when the organic carbon flux was high (Lean & McCave, 1998). Based on data from lake and marine sediments, Egli (2004) suggested that there are generally two coercivity components of magnetofossils; biogenic soft (BS) and biogenic hard (BH). The mean coercivities of BS and BH are around 40–50 mT and 60–80 mT, respectively. BS and BH often correlate with isotropic and elongated biogenic magnetite, respectively (Lascu & Plank, 2013; Yamazaki, 2012; Yamazaki & Ikehara, 2012). Egli (2004) also showed that magnetofossils in marine sediments generally have lower coercivity than those in lake sediments, although the number of marine samples considered in this comparison was limited.

Magnetic measurements of whole-cell magnetic bacteria show a broader range of coercivities that depends on both species and environmental conditions (Li, Menguy, et al., 2020, and references therein). The lowest observed coercivity of remanence (H_{cr}) is $\mu_0 H_{cr} \approx 10$ mT (Li et al., 2012), where μ_0 is the magnetic constant. We can estimate the lower limit of the coercivity by considering an ensemble of spherical grains. The hysteresis properties of SSD grains with cubic magnetic anisotropy were numerically evaluated by Joffe and Heubregbr (1974); H_{cr} was:

$$\mu_0 H_{cr} \approx \begin{cases} 0.296 \dfrac{K_1}{M_s} & (K_1 > 0) \\ 0.181 \dfrac{-K_1}{M_s} & (K_1 < 0) \end{cases} \tag{1}$$

where K_1 is the first-order anisotropy constant and M_s the saturation magnetization. Substituting the properties of magnetite ($M_s = 480$ kA/m and $K_1 = -13.5$ kJ/m) and maghemite ($M_s = 375$ kA/m and $K_1 = 4.7$ kJ/m) gives $\mu_0 H_{cr} = 11.5$ and 8.3 mT, respectively. These values suggest that the lowest coercivity of magnetic bacteria (Li et al., 2012), which was reported for microaerophilic *M. magneticum* AMB-1 cultured under oxic conditions, was due to the presence of non-chained, isotropic grains. This inference is consistent with microscopic observations of bacterial cells (Olszewska-Widdrat et al., 2019).

Several studies have shown that pelagic clayey sediment (so-called red clay) contains abundant magnetofossils (Shimono & Yamazaki, 2016; Usui et al., 2017, 2019; Yamazaki & Ioka, 1997; Yamazaki & Shimono, 2013; Yamazaki et al., 2020). Red clay is deposited in oligotrophic regions below the carbonate compensation depth, and is generally barren of microfossils. Magnetofossils are promising indicators of paleoenvironment in such sediment. Furthermore, red clay is oxic, while many magnetic bacteria are microaerophilic to anaerobic (e.g., Bazylinski & Williams, 2006; Faivre & Schuler, 2008; Lefèvre & Bazylinski, 2013). Therefore, the magnetofossils in red clay may be produced by unknown species or under high-stress conditions. The reason bacteria in red clay produce magnetosomes is unclear because magnetotaxis along the geomagnetic field is unlikely to be advantageous in oxic sediment (Yamazaki & Shimono, 2013). Existing data indicate
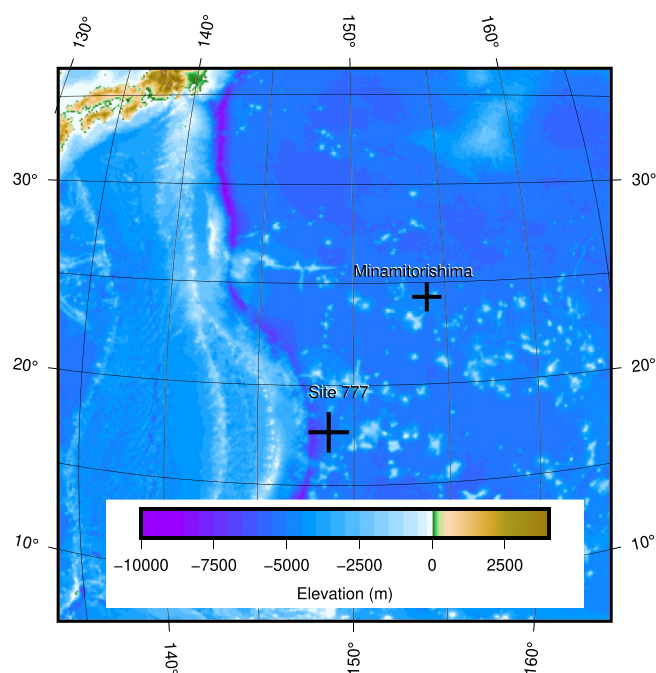
Figure 1. Map showing Ocean Drilling Program (ODP) Site 777 and the reference site Minamitorishima Island. The figure was produced by GMT6 (Wessel et al., 2019). The background topography is ETOPO1 (Amante & Eakins, 2009).

that the major morphotype of biogenic magnetite in red clay is isotropic (octahedral) (Shimono & Yamazaki, 2016; Usui et al., 2017; Yamazaki & Shimono, 2013; Yamazaki et al., 2020); occasionally bullet-shaped magnetite dominate (Usui et al., 2017; Yamazaki et al., 2020), possibly reflecting less-oxic conditions (Yamazaki et al., 2019). Octahedral and bullet-shaped magnetofossils in red clay are characterized by a mean coercivity of 15–25 mT and 30–40 mT, respectively (Usui et al., 2017; Yamazaki et al., 2020). These coercivities are clearly lower than the BS and BH components (Egli, 2004), respectively. This difference may be due to pervasive maghemitization, but may also reflect differences in species or environmental stresses. However, the number of studies of magnetofossils in red clay is still small, and it is unclear whether the data are globally representative.

Magnetic minerals in pelagic sediment have also been used to study eolian inputs. In the central North Pacific, the relative concentration of biogenic magnetite to detrital magnetic minerals decreased from ~2.6 to 1 Ma (Yamazaki & Ioka, 1997), which has been attributed to the increased eolian flux from East Asian deserts. Zhang and Liu (2018) argued that the signals of detrital magnetic minerals may be obscured by volcanic and biogenic magnetite. They estimated the concentration of high coercivity antiferromagnetic minerals (i.e., hematite and goethite) through reflectance measurements at Ocean Drilling Program (ODP) Site 885/886. Their data suggest a stepwise increase in eolian flux at around 2.6 Ma, superimposed on a generally increasing trend from ~3.5 to 2.5 Ma (Zhang & Liu, 2018; Zhang et al., 2020). This is consistent with the eolian flux estimated by chemical leaching at the same site (Rea et al., 1998). With respect to longer term variation, Yamazaki et al. (2020) proposed a sharp decrease in the relative concentration of biogenic magnetite near the Eocene-Oligocene boundary. This may be related to global cooling and increased eolian flux at that time. Such a trend is not fully consistent with a long-term record of eolian flux from the central Pacific (Janecek & Rea, 1983), which suggests an increase from ~25 Ma, but this inconsistency may be due to the age uncertainties (Usui & Yamazaki, 2021).

This study reports the variation in magnetic components in sediment from ODP Site 777 in the western North Pacific. We identify a previously unrecognized low coercivity mineral component and constrain its biogenic origin using magnetic and microscopy observations.

2. Materials

ODP Site 777 is located in the northern Mariana Basin at 17°42.2′N, 148°41.8′E (Figure 1) (Shipboard Engineering and Scientific Parties, 1990). The site location coincides with Deep Sea Drilling Project (DSDP) Site 452. Unconsolidated sediment was recovered almost continuously at Hole 777B, and we studied samples from this Hole. Sediment from Hole 777B was divided into two lithostratigraphic units, Unit I (0–30.4 m) and Unit II (30.4–36.7 m); Unit I was subdivided into Subunit IA (0–3.5 m) and Subunit IB (3.5–30.4 m). Subunit IA is biosiliceous clay, with the siliceous fossil content decreasing with depth. Subunit IB is brown hemipelagic clay. Unit II is pelagic light brown clay interlayered with dark brown clay. Shipboard paleomagnetic results suggested that Unit I was deposited during ~12–0 Ma with the sedimentation rate increasing from 0.6 mm/kyr at the bottom to 8 mm/kyr at the top (Shipboard Engineering and Scientific Parties, 1990). Unit II also shows possible geomagnetic reversals; however, the boundary between Units I and II may be a hiatus, so the age of Unit II is unclear. Unit II is underlain by chert, and chert from DSDP Site 452 was dated as Campanian based on radiolarians (Kling, 1982).

Samples were taken from Hole 777B every ~25 cm using 20 cm^3 plastic scoops (2 cm width). We separated about 1 cm^3 of wet sediment from each sample for this study, so depths have a 2 cm uncertainty.

3. Methods

3.1. Rock Magnetism

We placed sampled wet sediment into plastic cubes for magnetic measurements. Anhysteretic remanence (ARM) was imparted and measured using a pass-through cryogenic magnetometer (2G Enterprises Model 755R) with in-line coils. The peak alternating field was 80 mT, and the DC field was 0.1 mT. The decay rate of the alternating field was controlled by the software package 2G Long Core using the parameters; degaussing velocity: 8 and ramp rate: 3. Saturation isothermal remanence (SIRM) was imparted at 2.7 T using a pulse magnetizer (2G Enterprises Model 660) and measured with a spinner magnetometer (Natsuhara Giken, ASPIN). The ratio of the susceptibility of ARM to SIRM (k_{ARM}/SIRM) was calculated. k_{ARM}/SIRM reflects both grain size and magnetostatic interactions (Cisowski, 1981). In pelagic sediments, high k_{ARM}/SIRM often reflects low magnetostatic interactions caused by abundant magnetofossils (Usui et al., 2017; Yamazaki, 2008; Yamazaki & Shimono, 2013).

Hysteresis was measured using a vibrating sample magnetometer (VSM: Princeton Measurements Model 29/3902). Major loops were measured between ±1 T to estimate the ratio of saturation remanence to saturation magnetization (M_{rs}/M_s) and coercivity (H_c). The loops were processed with HystLab (ver. 1.0.1; Paterson et al., 2018) for loop centering, drift correction, and paramagnetic correction. Paramagnetic corrections were based on high field linear slope subtraction. Backfield demagnetization of isothermal remanence (IRM) imparted by 1 T was measured to estimate H_{cr}.

We estimated IRM coercivity components using Max UnMix (ver. August-1-2019; Maxbauer et al., 2016). The backfield demagnetization curves were interpolated using cubic splines and rescaled to provide normalized IRM acquisition curves. The gradient of IRM acquisition curves was decomposed into a collection of skewed normal distributions; $w (B; B_h, DP, S)$ (Egli, 2003; Fernández & Steel, 1998). Parameter B_h controls the location of the distribution, DP the dispersion, and S the skewness ($S < 1$ for right-skewed distributions). The contribution (OC) of each component in a sample is defined as:

$$\text{IRM(1T)} = c \sum_i \left(OC_i \int_0^{1\text{T}} w_i(B) dB \right) \qquad (2)$$

where the scaling factor c is determined so that the sum of OC is 1. Before processing, we removed data points at ~31.6, ~33.6, ~100.4, ~105.7, and ~111.1 mT because of systematic jumps in the magnetization that we suspected to be machine errors. The results of Max UnMix are sensitive to the initial fits. Thus, we used principal component analysis (PCA) of the IRM acquisition curves to constrain initial fits. PCA is one of the so-called unsupervised unmixing, which derives fixed endmembers from sample data to describe the behavior of a set of samples (Heslop, 2015). More sophisticated unsupervised methods are sometimes used to estimate physically realistic endmembers (Heslop & Dillon, 2007), but here we used simple PCA, as we only need initial fits for Max UnMix. We extrapolated trends in the principal component (PC) space to estimate mixture endmembers. Endmembers were decomposed using Max UnMix to obtain skewed normal components. We used these skewed normal components, with slight adjustments for each sample, as initial fits to decompose the IRM acquisition curves.

First-order reversal curves (FORCs) were also measured on the cube samples using the VSM. Measurements were conducted with the parameters; Hb1: −15 mT, Hb2: 15 mT, Hc1: 0 mT, Hc2: 80 mT, Hsat: 500 mT, and field steps of 0.5 mT (231 FORCs). FORC distributions (Pike et al., 1999; Roberts et al., 2000) were estimated and analyzed using VARIFORC (ver. 4.02; Egli, 2013) with smoothing parameters; $s_{b0} = 4$, $s_{c0} = s_{b1} = s_{c1} = 5$, and $\lambda_b = \lambda_c = 0.1$ and a central ridge vertical offset of 0.3 mT. For complete FORC parameters, see the data availability statement. After the magnetic measurements, selected samples (~1 in 2) were freeze-dried and weighed to calculate mass-normalized SIRM and k_{ARM}.

3.2. Microscopy

Magnetic mineral extracts of one sample from each of Unit I (18.5 m) and Unit II (35.5 m) were investigated with a transmission electron microscope (TEM). We tested two extraction methods. The first was to circulate the dispersed sediments through a high magnetic field gradient, referred to here as the "circulation

method." The second was the "magnetic finger" method (Kirschvink et al., 1992; Petersen et al., 1986; Von Dobeneck et al., 1987). For comparison, we also performed extractions on a red clay sample taken proximal to Minamitorishima Island (KR13-02 PC06, 6.525 m) (Yamazaki et al., 2020). We evaluated extraction efficiency by comparing SIRM of bulk specimens and extracts; it was around 40 % for the circulation method. The efficiency of the magnetic finger method was 61 % for the Unit I sample, 64 % for the Unit II sample, and 68 % for the sample from Minamitorishima Island. The magnetic extracts were dispersed in ethanol. A small drop of the suspension was dried on a carbon-coated copper grid and analyzed using a TEM operated at 120 kV (JEOL JEM-1400) at the Atmosphere and Ocean Research Institute, The University of Tokyo. We identified biogenic magnetite based on characteristic morphology (octahedron, hexagonal prism, or bullet) and grain sizes restricted to the SSD range of magnetite (Kopp & Kirschvink, 2008). To evaluate grain morphology quantitatively, we measured the length and width of ~400–1,000 grains of biogenic magnetite in each sample. The morphology measurements were performed on the extract prepared by the circulation method. Further, we also examined the 35.5 m sample extracted by the magnetic finger method. We assigned biogenic magnetite into three categories: isotropic (width/length > 0.7), elongated (width/length < 0.7), and bullet-shaped. Because magnetization depends on total volume rather than the number of grains, we estimated the volume distribution as $q(s_i) = p(s_i)s_i^3$, where s is the size of a grain defined as (width + length)/2, s_i is the mean size for a bin, and p is the frequency distribution of s.

3.3. Ferromagnetic Resonance

Ferromagnetic resonance (FMR) is sensitive to the magnetic anisotropy of SSD particles, and it has been used to detect and classify magnetofossils (e.g., Blattmann et al., 2020; Kopp et al., 2006; Kumagai et al., 2018; Usui et al., 2019; Weiss et al., 2004a). We measured FMR on one Unit II sample (36.5 m). Dried sediment was packed into a quartz tube and measured using a spectrometer (JEOL JES-RE2X) at the Department of Chemistry, Tohoku University. The microwave frequency was about 9.4 GHz (X-band), and the power was 1.0 mW. The applied magnetic field ranged from 0–800 mT.

3.4. Micromagnetic Simulations

Micromagnetic simulations were conducted using the MERRILL software package (ver. 1.3.5; Conbhuí et al., 2018). We used octahedral morphology where faces are {111}. Based on the TEM observations, we modeled grains with a volume of (35 nm)^3 and 15 % elongation along <111> (Supporting Information Figure S1). TEM images suggest that some grains may be truncated, but we did not consider truncation in the simulations. We also considered chains aligned along <111>. Each crystal in a chain was rotated by 60° about <111> relative to the neighboring crystals to match {111} faces (Supporting Information Figure S1) (Abraçado et al., 2011). The number of grains in a chain (*N*) was set between 1 and 10. The spacing between grains was 10 or 20 nm, which correspond to the longest observed spacings (Berndt et al., 2020). For comparison, we also simulated $N = 10$ with 5 nm spacing, $N = 1$ without elongation, and $N = 10$ with truncation without elongation. The model mesh was generated using Gmsh (ver. 4.7.1; Geuzaine & Remacle, 2009) with a target mesh size of 9 nm. The mesh was then converted to PATRAN format using Python package meshio (ver. 4.3.8; https://github.com/nschloe/meshio) and a MATLAB routine merrillsavepat.m. We modeled maghemite and magnetite because magnetofossils in pelagic sediments are expected to be oxidized, as indicated by X-ray diffraction (Vali & Kirschvink, 1989) and the absence of a Verwey transition (Shimono & Yamazaki, 2016; Usui et al., 2018). Although magnetite sometimes exhibits partial maghemitization (e.g., Smirnov & Tarduno, 2000; Torii, 1997), we only considered pure magnetite and maghemite. For maghemite, we used the parameters: $A = 13$ pJ/m, $M_s = 375$ kA/m, and $K_1 = 4.7$ kJ/m^3 (Solov'yov & Greiner, 2009) where A is the exchange constant. For magnetite, we used parameters prescribed by MERRILL for 20°C. Bulk hysteresis parameters were estimated by averaging magnetization curves calculated for a field along 100 random directions (Berndt et al., 2020). Major hysteresis loops were calculated from −200 to 200 mT. Backfield demagnetizations of IRM imparted by 200 mT were calculated to −200 mT. M_{rs}/M_s, H_c, and H_{cr} were estimated by interpolation using cubic splines.
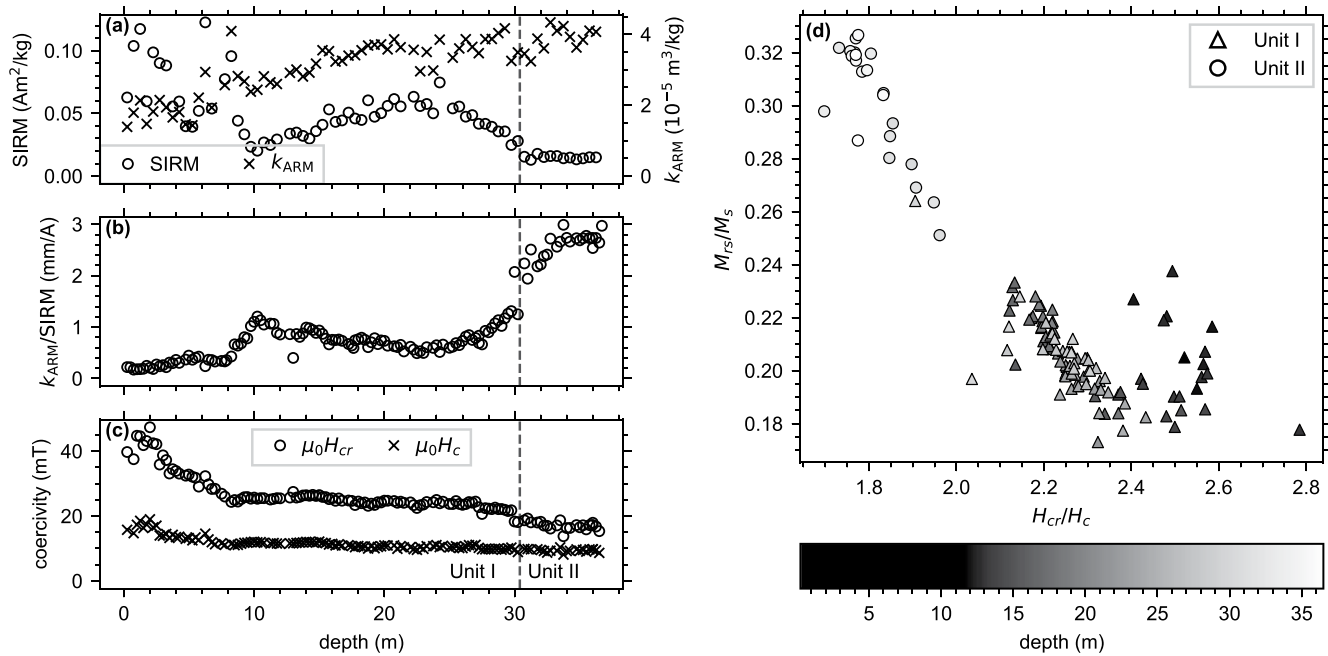
Figure 2. (a)–(c)Depth profiles of (a) Saturation isothermal remanence (SIRM) (circles) and k_{ARM} (crosses), (b)k_{ARM}/SIRM, and (c) coercivity of remanence (circles) and coercivity (crosses). Vertical dashed lines indicate the boundary between Units. (d) Day plot showing hysteresis parameters. Triangles represent Unit I data, and circles represent Unit II data. Fill colors indicate sample depths.

4. Results

4.1. Rock Magnetism

Units I and II show contrasting magnetic properties. Additionally, depths of ~10 and ~5 m also exhibit marked changes in magnetic properties. SIRM (Figure 2a) is stable at ~0.02 Am^2/kg in Unit II (≥30.4 m). In Unit I, SIRM increases gradually up-core to ~0.06 Am^2/kg at ~24 m and decreases to ~0.02 Am^2/kg at ~10 m. SIRM increases rapidly to ~0.1 Am^2/kg at ~8 m, followed by a rapid decrease to ~0.04 Am^2/kg at ~5 m. SIRM increases again toward the core top to ~0.1 Am^2/kg. Variation of k_{ARM} (Figure 2a) is distinct from SIRM. It is stable at ~3.8×10^{-5} m^3/kg below 20 m. It gradually decreases up-core to ~1.8×10^{-5} m^3/kg at ~5 m, and is then stable to the core top. k_{ARM}/SIRM ranges from 0.18 to 3.0 mm/A (Figure 2c). Unit II shows high k_{ARM}/SIRM (>2.2 mm/A) below 31 m, which is comparable to red clay dominated by magneto-fossils (Shimono & Yamazaki, 2016; Usui et al., 2017, 2019; Yamazaki & Shimono, 2013). Unit I shows lower values (<1.0 mm/A) except for the bottom 1.5 m (28.5–30 m), where the values are transitional between the two Units. The upper ~10 m is characterized by the lowest values of <0.5 mm/A.

Hysteresis properties are summarized in the Day plot (Day et al., 1977) (Figure 2d). Data are in the "pseu-do-single domain" range (Day et al., 1977; Dunlop, 2002), but Unit II samples plot closer to the SSD region. H_c and H_{cr} both increase up-core (Figure 2c). They are ~10 mT and ~15 mT, respectively, in Unit II. In Unit I, they increase rapidly in the upper 9 m.

IRM gradient curves are shown in Figure 3. Unit II is characterized by a near-zero gradient above 100 mT (Figure 3c). The derivative mode is at ~28 mT, but the curves also include a hump at ~10 mT. In contrast, the Unit I curves (Figures 3a and 3b) have a non-zero gradient above 100 mT and lack a hump at low fields. Between 10 and 30 m, the IRM gradient curves vary little with a mode at ~28 mT (Figure 3b). From ~10 m, the modal coercivity increases up-core and reaches ~50 mT at the core top (Figure 3a).

Three PCs (PC1, PC2, and PC3) explain 99.9 % of the variance of the IRM curves. In PC space there are two linear trends spanning 0–6.25 m and ≥30 m (Figure 4). These samples can therefore potentially be represented by the mixing of two endmembers for each trend. Samples from 8.5–30 m appeared to form a cluster, and samples above this depth (6.5–8.25 m) may be transitional. The trend for 0–6.25 m shows depth
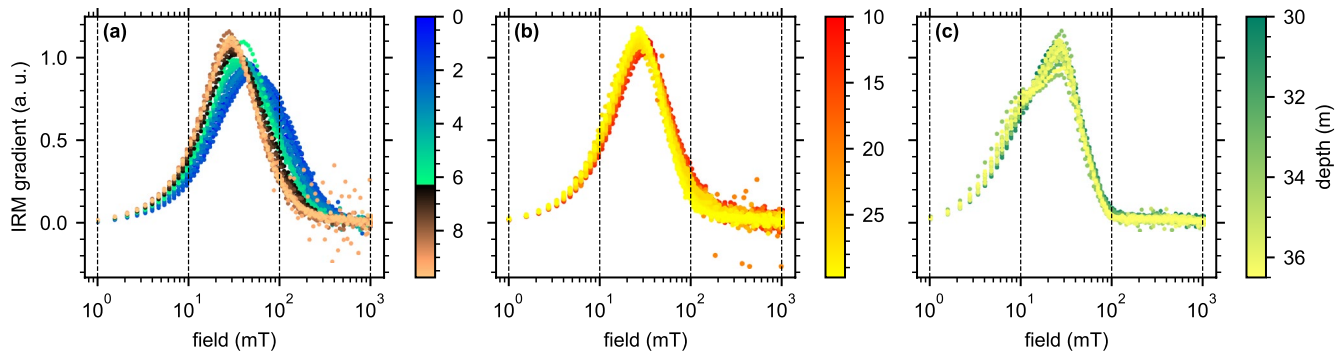
Figure 3. Isothermal remanence (IRM) gradient curves of (a) < 10 m, (b) 10–30 m, and (c) ≥30 m. Curves are normalized by IRM at 1 T. Data colors indicate sample depths using the same color scale as Figure 4.

progression, while that for ≥30 m does not. To estimate the endmembers, we fit a line to each linear trend using PCA (Supporting Information Figures S2 and S3). We found that extrapolation of these lines resulted in narrowing the endmember coercivity distributions until they start to show negative values. We selected distributions just before they started to show significant negative values as endmembers; EM I-1 and EM I-2 for 0–6.25 m trend, and EM II-1 and EM II-2 for ≥30 m (Figures 4d–4f). The endmembers were fitted with skewed normal distributions using Max UnMix (Figures 5a–5d). The endmember fitting parameters are
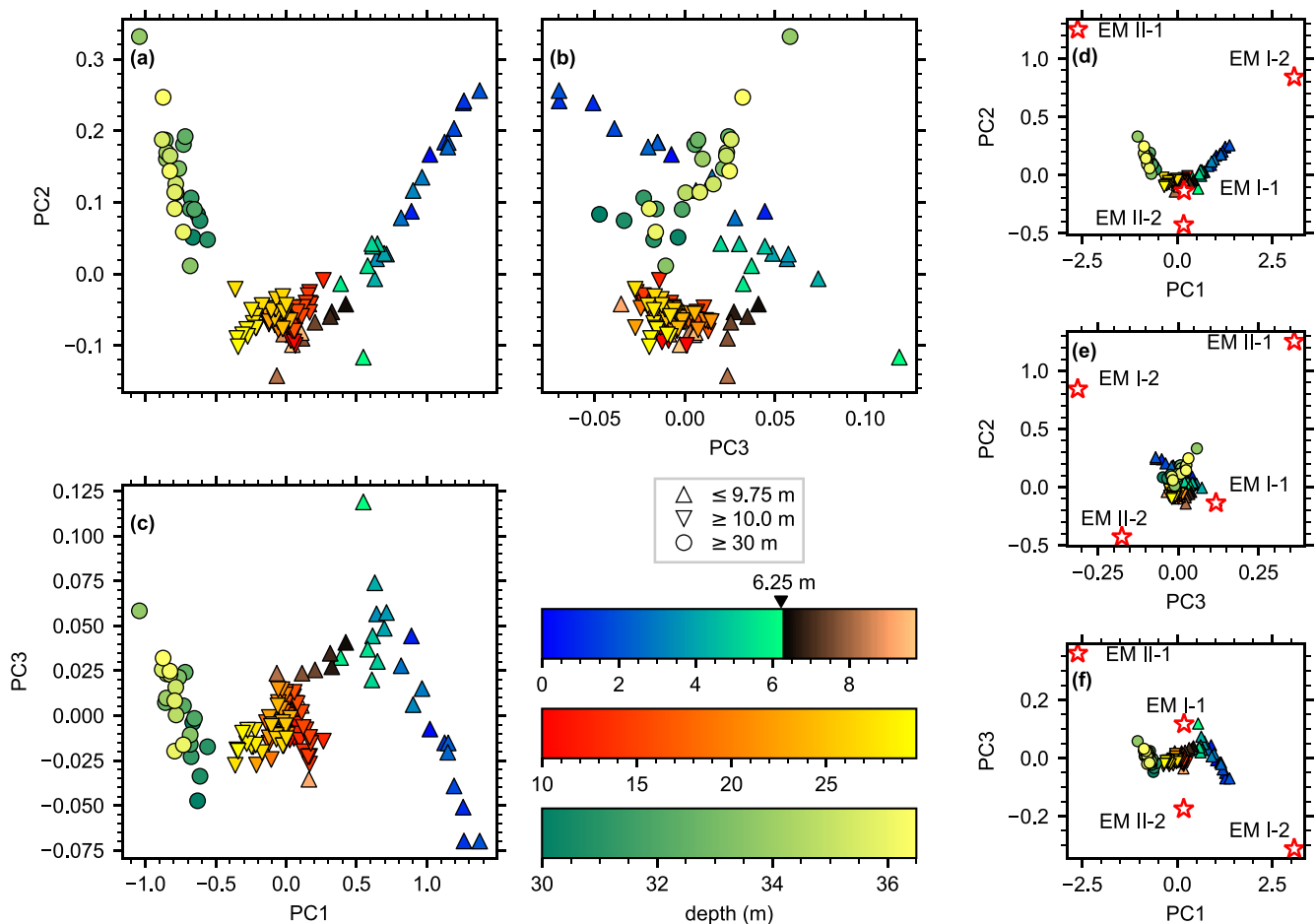

Figure 4. Results of the principal component analysis (PCA) of the isothermal remanence (IRM) curves. (a)–(c) IRM curves in the three-PC space projected on orthogonal planes. (a) PC2 against PC1. (b) PC2 against PC3. (c) PC3 against PC1. (d)–(f) Same as (a)–(c) with endmembers shown as red stars. Triangles represent samples above 10 m, inverted triangles samples at and below 10 m, and circles samples at and below 30 m. Colors indicate sample depths.
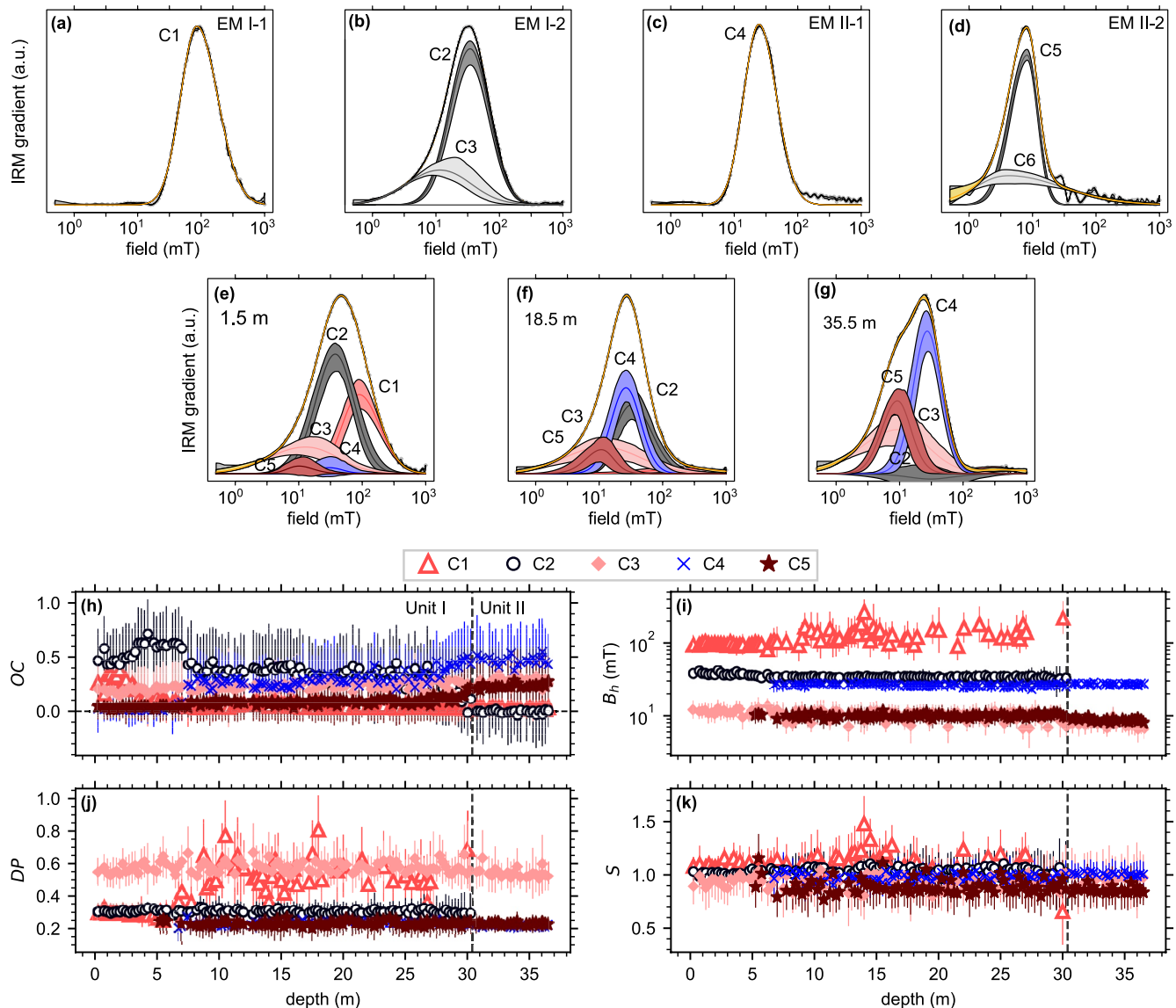
Figure 5. Results of the isothermal remanence (IRM) decomposition. (a)–(d) Fitting of PC endmembers. (e)–(g) Fitting examples of the IRM gradient of the samples. Gray circles show estimated gradients, and orange curves show the sum of fitted components. Shaded areas represent 95% confidence intervals obtained by 100 Monte-Carlo resamplings in Max UnMix. (h)–(k) Depth profiles of the fitting parameters. Red triangles represent C1, blue circles C2, pink diamonds C3, blue crosses C4, and red stars C5. Error bars show standard deviations multiplied by 2. (h) Relative contribution to the total IRM at 1 T (OC). (i) Location parameter, B_h. (j) Dispersion parameter, DP. (k) Skewness parameter, S. In (i)–(k), only components with the mean $OC > 0.05$ are plotted.

listed in Table 1. EM I-2 and EM II-2 were fitted by two distributions, and the large DP distributions from each were similar. Thus, we consider them to be the same component. As a result, we obtained five skewed normal components (C1–C5) to act as starting distributions in Max UnMix. We note that the coercivity components for 6.5–30 m are not well constrained by the IRM data alone (Figure 4). Nonetheless, stratigraphically, this interval is located in the middle part of the core, and the data are positioned between the two linear trends. The simplest explanation for these observations is that this interval represents a transition from one trend to the other. Consequently, we decided to use C1–C5 as the starting distributions for these samples. Each IRM acquisition curve was first manually fitted based on the selected initial distributions, and then the fit was optimized automatically using Max UnMix.

The results of the IRM decomposition are presented in Figure 5 and Supporting Information Table S1. The fitting parameters are stable with respect to depth. The DP of C1 has a large scatter in samples where this

Table 1
IRM Components Obtained by PCA

Name	B_h (mT)	DP	S	Comments
C1	97.7	0.29	1.13	
C2	33.6	0.31	0.98	
C3	10.6	0.50	0.95	
C4	26.1	0.26	1.07	
C5	6.8	0.22	0.78	
C6	7.5	0.72	1.31	Merged with C3

Abbreviations: IRM, isothermal remanence; PCA, principal component analysis.

component only makes a small contribution. Therefore, such scatter may simply represent uncertainty in the unmixing process. Note that Max Un-Mix does not force *OC* to be positive. Negative values were estimated for components with small contributions, but this does not affect the major components. The stability in the fitting parameters partly supports the validity of the five-component unmixing. In particular, it validates treating C6 and C3 as the same component. We found that a slightly smaller *DP* for C4 (~0.21) and larger B_h for C5 (~9 mT) than those obtained from PCA (Table 1) yielded better fits (Figures 5i and 5j). High contributions of C4 and C5 characterize Unit II (Figure 5h). The co-existence of these relatively narrow (small *DP*) components explains the hump seen in the IRM curves at ~10 mT (Figure 3c). The contributions of C4 and C5 are smaller in Unit I and virtually absent above ~7 m. Unit I shows a higher contribution of C2. C1 starts to increase from ~5 m and rapidly increases across 3.5–2 m. C1 remains high in the top 2 m. The contribution of C3 gradually decreases up-core from ~25 to ~20%.

FORC distributions in Unit II are concentrated around $H_b = 0$, forming central ridges (Figure 6c, Supporting Information Figure S4). In Unit I, the FORC distributions have a greater vertical spread (Figures 6a and 6b), suggesting the increased contribution of the interacting SSD and "pseudo-single-domain" particles (Harrison & Lascu, 2014; Roberts et al., 2000, 2017). The relative contribution of the central ridge decreases up-core (Supporting Information Figure S4). The central ridge coercivity distribution (Egli, 2013; Egli et al., 2010) of Unit II samples contains a hump at ~10 mT and a peak at ~25 mT (Figure 6e), similar to the IRM gradient (Figure 3c). Because the central ridges represent the contribution from non-interacting SSD-like particles, this similarity indicates that IRM components C4 and C5 are carried by non-interacting SSD-like particles. Unit I samples do not show a clear low field hump (Figure 6d).

4.2. Microscopy

All examined samples contain abundant biogenic magnetite (Figures 7a–7d); the sample from Unit I contains a larger proportion of irregularly shaped grains of probable detrital origin. The circulation and
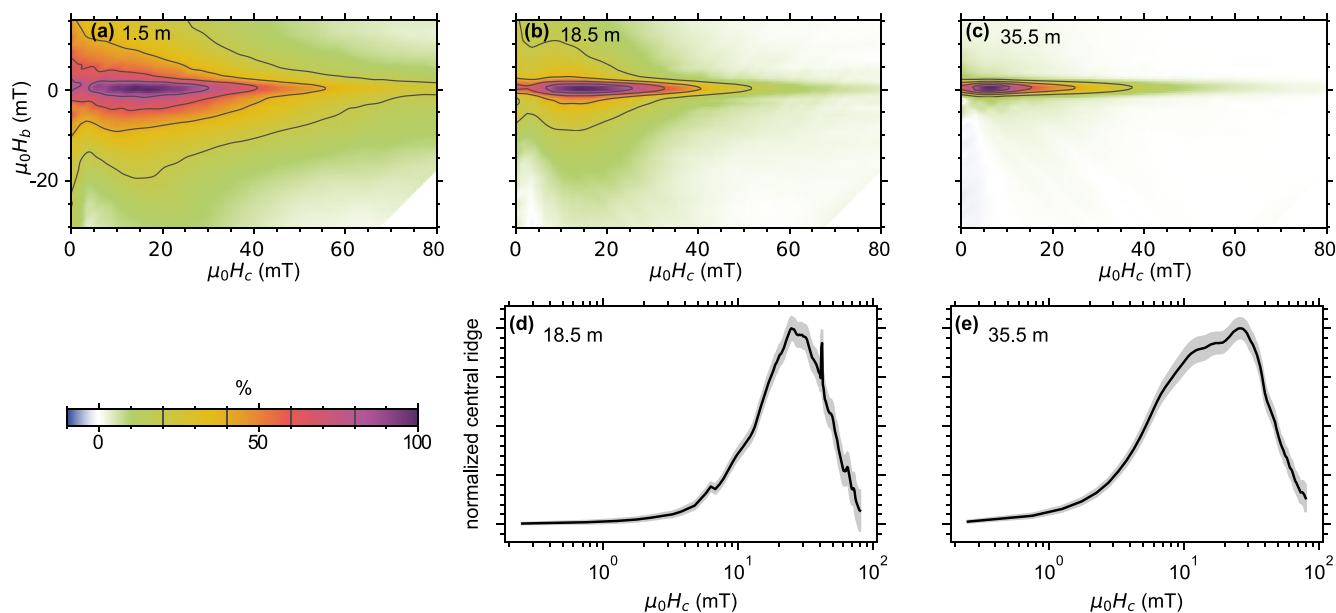

Figure 6. (a)–(c) Representative First-order reversal curves (FORC) distributions. Contours are at 20, 40, 60, and 80%. (a) Unit I sample from 1.5 m. (b) Unit I sample from 18.5 m. (c) Unit II sample from 35.5 m. Central ridge coercivity distribution for 18.5 m (d) and 35.5 m (e). Shaded areas represent standard errors multiplied by 2.
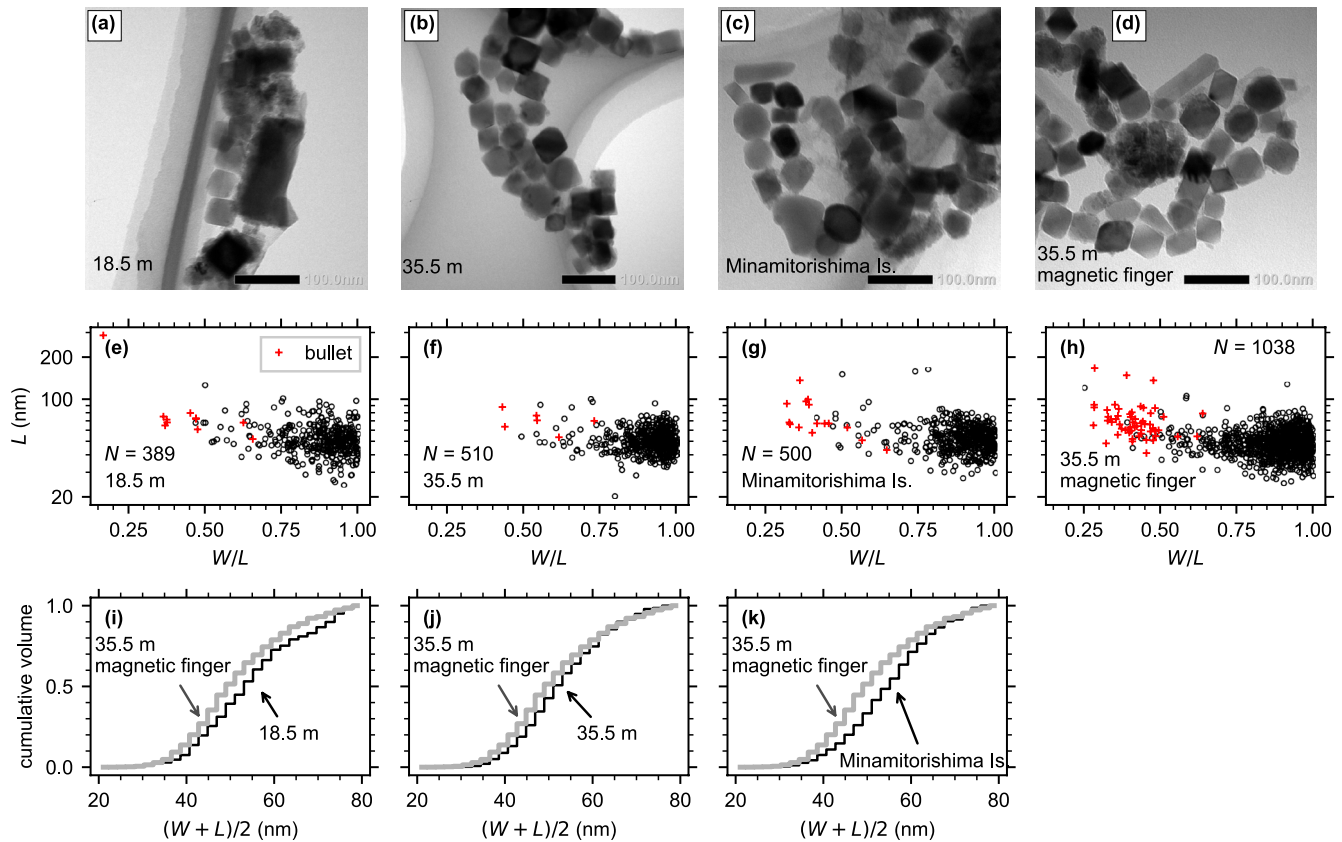
Figure 7. (a)–(d) Representative transmission electron microscope (TEM) images of (a) 18.5 m, (b) 35.5 m, (c) KR13-02 PC06 6.525 m, and (d) 35.5 m extracted by the magnetic finger method. (a)–(c) were extracted by the circulation method. Scale bars are 100 nm. (e)–(h) Scatter plots showing length (L) versus the ratio of width (W) over L of biogenic magnetite observed under the TEM. Circles represent isotropic and elongated grains, and red crosses bullet-shaped grains. (i)–(k) Cumulative volume distribution of size ($W + L$)/2 for (i) 18.5 m, (j) 35.5 m, and (k) KR13-02 PC06 6.525 m. Gray curves represent the distribution for 35.5 m extracted by the magnetic finger method.

magnetic finger methods resulted in nearly identical size and shape distributions of biogenic magnetite (Figures 7b, 7d, 7f and 7j) even though the extraction efficiency was higher for the magnetic finger method. In the Unit II sample extracted by the magnetic finger method, isotropic grains account for 87% of the biogenic magnetite, with 8% elongated grains and 5% bullet-shaped grains. The average grain size ((width + length)/2) of isotropic and elongated grains is 45.9 nm with standard deviation of 10.1 nm. The average elongation (length/width) is 1.17 with standard deviation of 0.21. The distributions of these parameters are similar in the Unit I and Unit II samples (Figures 7e, 7f, 7h, 7i and 7j). The Unit I and Unit II samples are also similar to the sample from Minamitorishima Island, except that the biogenic magnetite in the ODP Site 777 samples is slightly smaller (Figures 7i–7k). The biogenic magnetite in the Minamitorishima sample consists of 91% equant grains, 6% elongated grains, and 3% bullet-shaped grains. The average and standard deviation of the grain size of isotropic plus elongated grains are 50.2 and 12.0 nm, respectively, and the elongation mean and standard deviation are 1.15 and 0.18, respectively.
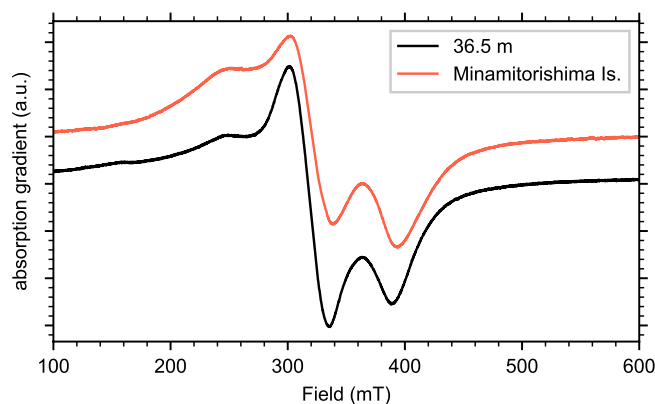
4.3. Ferromagnetic Resonance

Figure 8. Ferromagnetic resonance (FMR) spectrum of a sample taken from 36.5 m. The red curve is a reference spectrum from Minamitorishima Island core MR15-E01 PC12 6.15 m (Usui et al., 2019).

The FMR spectrum (Figure 8) is asymmetric, suggesting the presence of SSD-like grains with high anisotropy. It is nearly identical to the spectra from the red clay sediment around Minamitorishima Island, which

Table 2
Summary of Hysteresis Parameters Obtained From Micromagnetic Simulations

Phase	Spacing (nm)	N	M_{rs}/M_s	$\mu_0 H_{cr}$ (mT)	$\mu_0 H_c$ (mT)
magnetite	-	1	0.40	22.78	16.60
magnetite	10	2	0.42	45.03	38.96
magnetite	10	3	0.43	54.38	41.52
magnetite	10	6	0.43	58.09	50.45
magnetite	10	10	0.43	58.65	52.35
magnetite	20	2	0.41	33.95	29.21
magnetite	20	3	0.42	39.44	30.93
magnetite	20	6	0.42	40.52	35.88
magnetite	20	10	0.42	41.11	36.96
maghemite	-	1	0.53	11.51	6.08
maghemite	10	2	0.44	29.75	20.24
maghemite	10	3	0.44	31.26	24.79
maghemite	10	6	0.44	40.87	33.46
maghemite	10	10	0.44	41.28	34.03
maghemite	20	2	0.43	22.74	13.58
maghemite	20	3	0.43	23.89	17.59
maghemite	20	6	0.44	27.98	22.15
maghemite	20	10	0.44	28.04	22.72

contained abundant biogenic magnetite and could be fitted with a single anisotropy (Usui et al., 2019). We also calculated phenomenological parameters to characterize the FMR spectrum (Weiss et al., 2004a). We obtain an effective g-factor of 2.12 and an asymmetry ratio of 0.69. These values are consistent with the presence of magnetofossils (Chang et al., 2014; Kopp et al., 2006; Weiss et al., 2004a).

4.4. Micromagnetic Simulations

Simulation hysteresis parameters are summarized in Table 2 and Figure 9. For octahedra with 15% elongation, M_{rs}/M_s are over 0.399 for all cases, indicating uniaxial, near-SSD behavior. It is unclear why these are below the theoretical value of 0.5; simulations with 5 nm separation and truncated octahedra yield similar M_{rs}/M_s (Supporting Information Table S2). H_{cr} and H_c increased with N; for $N = 1$, $\mu_0 H_{cr} = 22.8$ mT for magnetite and 11.5 mT for maghemite. H_{cr} and H_c appeared to reach stable values by $N \approx 6$, which is consistent with previous studies (Berndt et al., 2020; Chang et al., 2019; Muxworthy & Williams, 2009). H_{cr}/H_c is large for maghemite when $N < 3$, indicating that these systems deviate from uniaxial SSD behavior.

5. Discussion

5.1. Carriers and Evolution of Magnetic Components

Changes in magnetic properties are observed around the boundary between Units (30.4 m), 10 m, and 5 m. Across the Unit boundary, magnetostatic interactions decrease up-core. Specifically, Unit II samples show high k_{ARM}/SIRM (Figure 2b) and have FORC distributions dominated by central ridges (Figure 6c). TEM observations in Unit II reveal abundant isotropic biogenic magnetite (Figure 7c). In combination, these results indicate that Unit II contains a higher proportion of biogenic magnetite than Unit I. In the IRM decomposition, the Unit boundary marks an up-core decrease in C4 and C5 and an increase in C2 (Figure 5h). The B_h and DP of C2 and C4 are similar to previously identified detrital and biogenic magnetite in pelagic sediments (Usui et al., 2017; Yamazaki, 2012; Yamazaki & Shimono, 2013). We interpret C2 and C4 to represent detrital and biogenic magnetite, respectively. Paleomagnetic data suggested that the Unit boundary is older than 12 Ma (Shipboard Engineering and Scientific Parties, 1990). This is consistent with the sharp drop in the relative biogenic magnetite contribution at around 35 Ma observed elsewhere in the Pacific (Yamazaki et al., 2020). We speculate that Unit II may be older than the Oligocene.

From 10 to 8 m, k_{ARM}/SIRM decreases up-core (Figure 2b). Although ~10 m corresponds to a change in trends in PC space (Figure 4), the relative contributions of the IRM components do not show a major change. We interpret this k_{ARM}/SIRM trend as subtle changes in detrital composition, with either up-core coarsening or an increase in magnetostatic interactions. From 8 m, biogenic C4 rapidly decreases, and detrital C2 increases up-core (Figure 5h). SIRM (Figure 2a) and sedimentation rate (Shipboard Engineering and Scientific Parties, 1990) generally increase up-core from around this depth. Thus, the flux of detrital magnetite must have increased. Paleomagnetic data suggest ages corresponding to ~3.6 Ma at 10 m and ~2.6 Ma at 8 m (Shipboard Engineering and Scientific Parties, 1990). At higher latitude ODP Site 885/886, eolian flux started to increase at ~3.6 Ma and reached a stable high by ~2 Ma (Rea et al., 1998). IRM analyses of this and other sites in the north Pacific suggest a further increase in dust flux at ~2.6 Ma (Yamazaki & Ioka, 1997; Zhang et al., 2020). Our data appeared to capture both events. However, the chronology is uncertain, and caution is required when attempting correlation with other sites. For example, the Matuyama chron seems to be too short, suggesting a short hiatus (Shipboard Engineering and Scientific Parties, 1990). Also, SIRM above 10 m exhibits a large scatter (Figure 2a), which may represent volcanic input from the nearby Mariana arc. Thus, further research is needed to clarify the variation of eolian inputs at ODP Site 777.
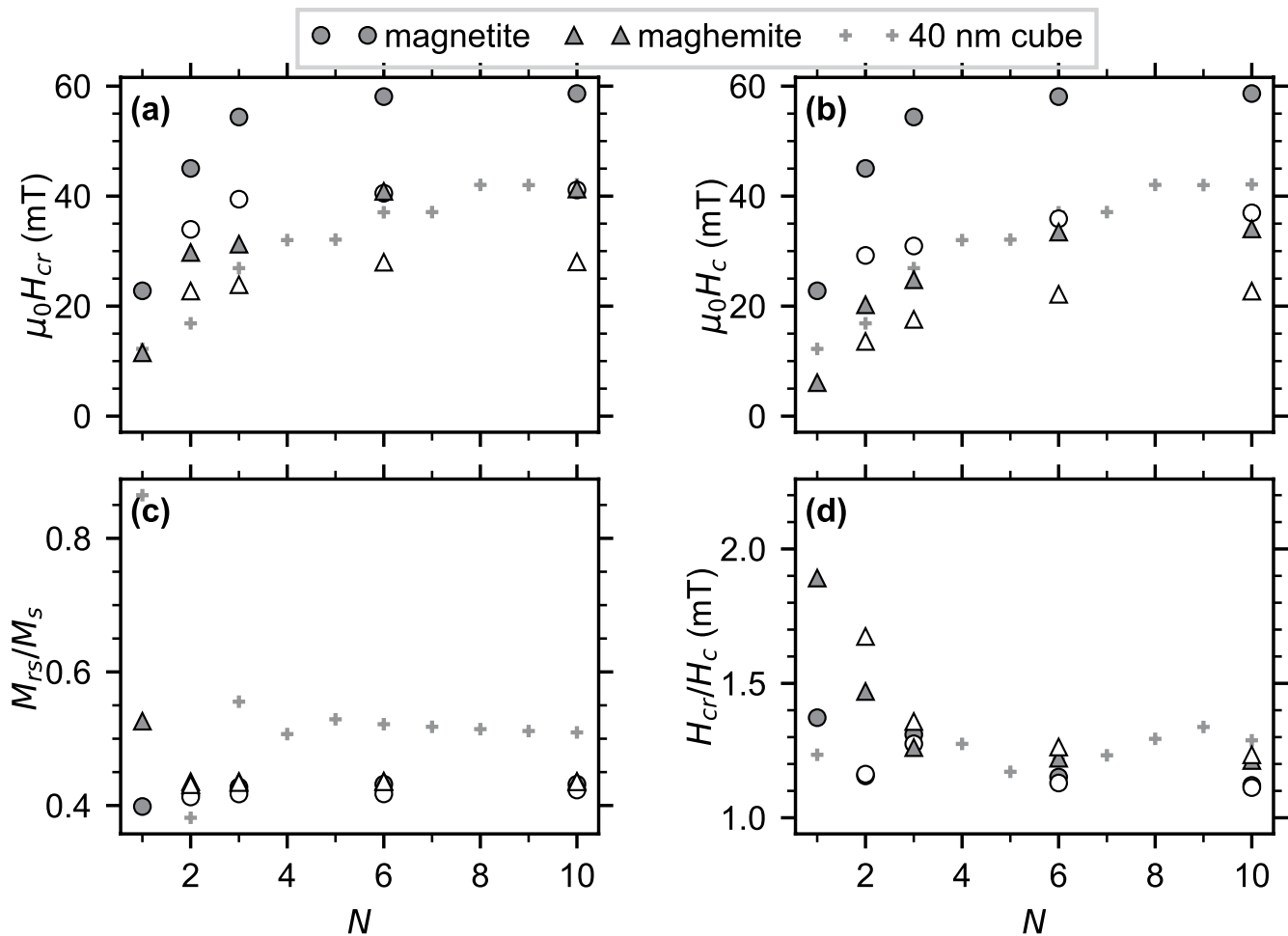
Figure 9. Results of micromagnetic calculations expressed as the dependence of hysteresis parameters on the number of grains per chain (N). Circles represent magnetite and triangles maghemite. Filled symbols are calculations with 10 nm grain separations, and open symbols are with 20 nm separations. Gray crosses are 40 nm magnetite cubes with 10 nm separations (Berndt et al., 2020). (a) Coercivity of remanence. (b) Coercivity. (c) Ratio of saturation remanence to saturation magnetization. (d) Coercivity ratio.

From around 5 m, IRM curves indicate an up-core increase in high coercivity phase(s) (Figure 3a), which corresponds to the increase in high coercivity component C1 (Figure 5h). The coercivity and dispersion of C1 ($B_h \approx 100$ mT, $DP \approx 0.3$) are similar to a detrital component observed in the North Pacific during the last ~0.9 Ma (Yamazaki, 2008; Yamazaki, 2009, 2012). This component may correspond to eolian ti-tanomaghemite (Yamazaki, 2008), hematite (Hu et al., 2013), or fine-grained titanomagnetite inclusions in silicate (Zhang & Liu, 2018). SIRM and sedimentation rate also increase up-core, implying that the flux of the high coercivity phase(s) has increased. Paleomagnetic data suggest the Brunhes-Matuyama boundary (0.77 Ma) occurs at 5.8 m (Shipboard Engineering and Scientific Parties, 1990). A coeval change in detrital magnetic minerals flux has not been reported at other sites (Yamazaki, 2012; Yamazaki & Ioka, 1997; Zhang & Liu, 2018; Zhang et al., 2020). Nevertheless, we emphasize that at least two distinct non-biogenic components, C1 and C2, are required to explain a linear trend for <6.25 m in the PCA results (Figure 4). Our data suggest that eolian dust composition has changed at ODP Site 777 since <0.8 Ma. This change may correspond to a gradual increase in eolian flux in the late Pleistocene (Hovan et al., 1991).

The above discussions indicate that IRM components C1, C2, and C4 represent detrital titanomaghemite/hematite/magnetic inclusions, detrital magnetite, and biogenic magnetite, respectively. The contribution of C3 does not show a major change with depth. A component with low B_h and large DP similar to C3 has often been observed in pelagic sediment, including red clay, siliceous ooze, and carbonate (e.g., Li, Liu, et al., 2020; Roberts et al., 2013; Yamazaki, 2012; Yamazaki & Shimono, 2013). The origin of this component

is not clear, although it is generally attributed to detrital minerals. In pelagic siliceous clay from the Central Pacific, Li, Liu, et al. (2020) identified a similar component, which they attributed to relatively coarse particles with a vortex state. However, at ODP Site 777, the contribution of C3 does not correlate with the other detrital components C1 and C2. In Unit II, the contributions of C1 and C2 are near-zero, while the contribution of C3 is higher than that in Unit I. Similarly, Shimono and Yamazaki (2016) reported that red clay in the South Pacific contained only a biogenic magnetite component and a C3-like component before ∼30 Ma. On the other hand, eolian grain size over the Pacific has generally increased since 50 Ma (e.g., Rea, 1994). Thus, we consider there is no simple mechanism by which coarse-grained detrital magnetic minerals can be concentrated in these red clays. Instead, we speculate that C3 in red clay may be related to the diagenetic degradation of other components, especially biogenic magnetite.

5.2. Non-Chained Biogenic Octahedra

IRM component C5 makes high contributions in Unit II (Figure 5h). C5 also has several distinct properties. It exhibits non-interacting SSD-like behavior, as shown by the central-ridge coercivity distribution of the FORC distributions (Figure 6e). C5 is characterized by a relatively sharp coercivity distribution with $DP \approx 0.21$ and a B_h as low as 8–9 mT, which is comparable to the theoretical $\mu_0 H_{cr}$ of spherical SSD magnetite and maghemite. These results indicate that C5 corresponds to isotropic SSD-like grains with relatively well-sorted size.

The composition of C5 can be further constrained by the TEM observations. In the TEM images of the Unit II sample, the only isotropic grains with sizes of tens of nm were octahedra (Figures 7b and 7d). The size and shape of these octahedra are similar to the biogenic magnetite in the Unit I and Minamitorishima samples, where a C5-like component was minor or absent. Nevertheless, quantitative considerations of the IRM and TEM observations indicate that octahedra are also responsible for C5. The IRM of the Unit II TEM sample was decomposed into C3 (potentially detrital magnetite), C4 (biogenic magnetite), and C5, with contributions of 32, 44, and 24 %, respectively (Supporting Information Table S1). In the TEM observations, the extraction efficiency was not 100% but still high (>60 %) with the magnetic finger method. Importantly, the efficiency was almost identical for the Unit I sample and the Minamitorishima sample, while the IRM components were very different. In the Unit I sample, C5 accounts for only 8 % of the IRM, and C2 (detrital magnetite) for 32 %. In the Minamitorishima sample, IRM is dominated by a C4-like biogenic component with a possible contribution from a C3-like component without a C5-like component (Usui et al., 2017; Yamazaki et al., 2020). Therefore, extraction efficiency for C2, C4, and C5 should be comparable, and the relative contributions of C4 and C5 in the Unit II sample (0.65:0.35) can be translated to the relative volume fractions in the extracts. These considerations suggest that >35 vol % of isotropic magnetite in the Unit II sample corresponds to C5. Note that 13 % (in terms of particle abundance) of biogenic magnetite in the Unit II sample was anisotropic, which may contribute to C4. The morphology of the octahedra in the Unit II samples is typical of biogenic magnetite in red clay. Based on the size, shape, and non-interacting SSD-like magnetic properties, we conclude that C5 reflects octahedral biogenic magnetite. In addition, its low coercivity suggests that C5 may correspond to non-chained particles.

Micromagnetic calculations further support the hypothesis of C5 corresponding to non-chained biogenic octahedra. Single crystals of maghemite with size and shape comparable to the observed grains can result in $\mu_0 H_{cr} = 11.5$ mT (Figure 9). Single crystals of magnetite or two-crystal maghemite chains resulted in a much higher coercivity. Partial maghemitization may increase coercivity relative to magnetite (Ge et al., 2014). Many magnetic bacteria produce magnetosomes with separations smaller than those modeled in this study, and smaller separations have been shown to increase coercivity (Berndt et al., 2020; Chang et al., 2019). This information indicates that C5 is carried by non-chained biogenic magnetite oxidized to maghemite. The threshold size between SSD and superparamagnetic behavior for maghemite (∼30 nm) (Moskowitz et al., 1997) is thought to be larger than that for magnetite (∼20 nm) (Muxworthy & Williams, 2009). Nevertheless, most of the observed octahedra are larger than 30 nm (Figure 7), so maghemitization would not strongly affect their SSD-like behavior.

An alternative hypothesis is that C5 reflects diagenesis, appears to be implausible. Magnetosomes outside their cells are expected to collapse into clumps due to magnetostatic attractions (e.g., Kobayashi et al., 2006). So, it is unlikely that the isolated octahedra were produced by diagenesis of chained biogenic magnetite.

Severely degraded magnetosomal chains can exhibit $\mu_0 H_{cr} \approx 14$ mT (Li et al., 2012); however, such degradation also significantly increases magnetostatic interactions. These degraded chains were characterized by k_{ARM}/SIRM ≈ 0.25 and the disappearance of the central ridge (Li et al., 2012), while C5-rich samples (>30 m) are characterized by the highest k_{ARM}/SIRM and clear central ridges (Figures 2 and 6). Thus, degraded chains are incompatible with the characteristics of C5. We consider that octahedra corresponding to C5 were non-chained even when held inside the cells.

Finally, the hypothesis that C5 corresponds to non-chained maghemite is consistent with the FMR results. Magnetic anisotropy of isolated maghemite octahedra should be sufficiently small to produce a near symmetric signal indistinguishable from the detrital contribution (e.g., Weiss et al., 2004a). This explains why the measured spectrum is indistinguishable from that of the Minamitorishima samples (Figure 8) (Usui et al., 2019), even though the Minamitorishima samples do not show an appreciable contribution of a C5-like component (Usui et al., 2017).

5.3. Paleoenvironmental Implications of Biogenic Magnetite in Red Clay

The environmental factors controlling the abundance of C5 are unclear. Magnetic bacteria producing non-chained magnetite were reported as a distinct strain (Li, Menguy, et al., 2020) or as a result of oxidative environmental stress (Li & Pan, 2012; Olszewska-Widdrat et al., 2019). Oligotrophic, oxic red clay represents an environment very different from conventional environments inhabited by magnetic bacteria. On the other hand, the lithology and depositional environment of Unit II are not special amongst red clays. Similar interbedding of light and brown clay was also reported around Minamitorishima (Usui et al., 2017; Tanaka et al., 2020). By extension, the environmental conditions resulting in the production of non-chained biogenic magnetite in red clay may not be special. Indeed, we detect a non-zero contribution of C5 in Unit I (Figure 5h), where the shape of the IRM acquisition curves did not show a clear sign of C5. Careful quantification of a C5-like component in red clay from other sites will help to reveal environmental factors controlling the abundance of non-chained biogenic magnetite in red clay. Biogenic magnetite is slightly smaller in the 35.5 m sample, where C5 is most abundant. This pattern resembles the smaller grain size of magnetosomes in AMB-1 under aerobic conditions than under anaerobic conditions (Li & Pan, 2012). We hypothesize that the order of environmental stress for magnetic bacteria was Unit II > Unit I > around Minamitorishima Island, and is reflected by smaller grain sizes and higher C5 contributions.

In micromagnetic simulations, the B_h of biogenic IRM component C4 (~25 mT) was reproduced by maghemite in long ($N > 6$) chains with 20 nm spacing or short ($N = 2$–3) chains with 10 nm spacing (Figure 9). Both 20 nm spacing and $N = 2$–3 are atypical of magnetic bacteria (Berndt et al., 2020). Taken at face value, this result suggests that the C4 magnetofossils, which are widespread in red clay (Shimono & Yamazaki, 2016; Usui et al., 2017; Yamazaki & Shimono, 2013; Yamazaki et al., 2020), were also produced by unknown bacteria or reflect high environmental stress. However, B_h of chained magnetofossils may be affected by chain degradation (Li et al., 2012). Further studies are needed to understand B_h of C4 quantitatively.

The variety of magnetofossils in red clay, including chained and non-chained octahedra and bullet-shaped grains (Usui et al., 2017; Yamazaki et al., 2020), suggests that there are a variety of magnetic bacteria. It remains enigmatic as to why these bacteria produce magnetosomes even though the vertical redox gradient is minimal.

5.4. Magnetofossil Identification and Paleomagnetism

Magnetic techniques have been used to aid magnetofossil identification and quantification. Chain identification has been proposed as a prerequisite of magnetofossil identification (Kopp & Kirschvink, 2008), and FORC and FMR are two widely used methods to detect chained magnetofossils. On the other hand, a recent demonstration of non-chained magnetosomes (Li, Menguy, et al., 2020), and the magnetofossils identified in this study confirmed that the chain identification prerequisite may lead to some magnetofossils going unrecognized. Specifically, our results provide a case that the absence of asymmetric FMR signature alone, which reflects the absence of chains, should not be considered evidence against the presence of magnetofossils (cf., Chang et al., 2014; Weiss et al., 2004b). A similar discussion would also apply to the quantification of biogenic magnetite. Previous IRM analyses of pelagic sediment did not consider a C5-like component

(Shimono & Yamazaki, 2016; Yamazaki, 2008, 2009, 2012; Zhang et al., 2018), and may have overlooked this component.

Relative concentration variations in non-chained versus chained magnetofossils may also affect paleomagnetic recording. The observed coercivity of C5 is < 1/3 of typical magnetofossils (Egli, 2004), and the total volume of an isolated octahedron is < 1/10 the volume of a chain. These differences suggest that remanence carried by isolated octahedra would be susceptible to (thermo) viscous overprint. Magnetofossil abundance has been shown to affect relative paleointensity estimates due to different acquisition efficiencies of NRM and ARM (Chen et al., 2017; Heslop et al., 2013; Ouyang et al., 2014; Yamazaki et al., 2013). We consider that the relative abundance of magnetofossils with distinct magnetic properties such as C4 and C5 would also affect paleointensity estimates.

6. Conclusions

Magnetic properties of red clay at ODP Site 777 revealed significant depth variations. PCA and IRM decomposition indicate that the IRM acquisition curves can be represented by five components C1–C5. We interpret C1 and C2 to be detrital components, and C4 corresponds to magnetofossils. C3 resembles detrital components identified in earlier studies; however, the absence of a positive correlation with C1 and C2 suggests that C3 may be a diagenetic component.

Based on the available magnetostratigraphy (Shipboard Engineering and Scientific Parties, 1990), the contribution of C2 increases from ∼3.6 Ma and that of C1 from <0.8 Ma. These timings are consistent with available eolian flux reconstructions.

The coercivity of C5 is low ($B_h < 10$ mT), but we interpreted this as a magnetofossil component. FORC distributions indicate that C5 corresponds to isotropic, non-interacting SSD-like grains. TEM observations show that the only grains that satisfy these constraints and exist in sufficient amounts within the samples are octahedral biogenic magnetite. Micromagnetic simulations quantitatively support the hypothesis that non-chained and oxidized octahedra can reproduce the observed low coercivity. Component C4 appears to correspond to chained octahedra.

The lithology and geology of ODP Site 777 red clay are similar to the studied samples that contained a minor C5 contribution. This suggests that non-chained octahedral magnetofossils may be widespread in red clay. Detection of a C5-like magnetic component from other sites may reveal environmental factors controlling the abundance of non-chained biogenic magnetite and their paleomagnetic recording characteristics.

Data Availability Statement

All data produced in this study are available in Supporting Information and in Zenodo repository (doi: https://10.5281/zenodo.4579925).

References

Abraçado, L. G., Abreu, F., Keim, C. N., Campos, A. P. C., Lins, U., & Farina, M. (2011). Magnetosome chain superstructure in uncultured magnetotactic bacteria. *Physical Biology*, *7*(4), 46016. https://doi.org/10.1088/1478-3975/7/4/046016

Amante, C., & Eakins, B. W. (2009). ETOPO1 arc-minute global relief model: Procedures, data sources and analysis. In *NOAA technical memorandum NESDIS NGDC* (Vol. 24, pp. 1–19). National Oceanic and Atmospheric Administration.

Bazylinski, D. A., & Frankel, R. (2003). Biologically controlled mineralization in prokaryotes. *Reviews in Mineralogy and Geochemistry*, *54*(1), 217–247. https://doi.org/10.2113/0540217

Bazylinski, D. A., & Williams, T. J. (2006). Ecophysiology of magnetotactic bacteria. In *Magnetoreception and magnetosomes in bacteria* (pp. 37–75). Springer.

Berndt, T. A., Chang, L., & Pei, Z. (2020). Mind the gap: Towards a biogenic magnetite palaeoenvironmental proxy through an extensive finite-element micromagnetic simulation. *Earth and Planetary Science Letters*, *532*, 116010. https://doi.org/10.1016/j.epsl.2019.116010

Blattmann, T. M., Lesniak, B., García-Rubio, I., Charilaou, M., Wessels, M., Eglinton, T. I., & Gehring, A. U. (2020). Ferromagnetic resonance of magnetite biominerals traces redox changes. *Earth and Planetary Science Letters*, *545*, 116400. https://doi.org/10.1016/j.epsl.2020.116400

Chang, L., Harrison, R. J., & Berndt, T. A. (2019). Micromagnetic simulation of magnetofossils with realistic size and shape distributions: Linking magnetic proxies with nanoscale observations and implications for magnetofossil identification. *Earth and Planetary Science Letters*, *527*, 115790. https://doi.org/10.1016/j.epsl.2019.115790

Chang, L., Harrison, R. J., Zeng, F., Berndt, T. A., Roberts, A. P., Heslop, D., & Zhao, X. (2018). Coupled microbial bloom and oxygenation decline recorded by magnetofossils during the Palaeocene–Eocene thermal maximum. *Nature Communications*, *9*(1), 4007. https://doi.org/10.1038/s41467-018-06472-y

Chang, L., Roberts, A. P., Winklhofer, M., Heslop, D., Dekkers, M. J., Krijgsman, W., et al. (2014). Magnetic detection and characterization of biogenic magnetic minerals: A comparison of ferromagnetic resonance and first-order reversal curve diagrams. *Journal of Geophysical Research: Solid Earth*, *119*(8), 6136–6158. https://doi.org/10.1002/2014jb011213

Chen, L., Heslop, D., Roberts, A. P., Chang, L., Zhao, X., McGregor, H. V., et al. (2017). Remanence acquisition efficiency in biogenic and detrital magnetite and recording of geomagnetic paleointensity. *Geochemistry, Geophysics, Geosystems*, *18*(4), 1435–1450. https://doi.org/10.1002/2016gc006753

Cisowski, S. (1981). Interacting vs. non-interacting single domain behavior in natural and synthetic samples. *Physics of the Earth and Planetary Interiors*, *26*(1–2), 56–62. https://doi.org/10.1016/0031-9201(81)90097-2

Conbhuí, P. Ó., Williams, W., Fabian, K., Ridley, P., Nagy, L., & Muxworthy, A. R. (2018). MERRILL: Micromagnetic earth related robust interpreted language laboratory. *Geochemistry, Geophysics, Geosystems*, *19*(4), 1080–1106. https://doi.org/10.1002/2017gc007279

Day, R., Fuller, M., & Schmidt, V. A. (1977). Hysteresis properties of titanomagnetites: Grain-size and compositional dependence. *Physics of the Earth and Planetary Interiors*, *13*(4), 260–267. https://doi.org/10.1016/0031-9201(77)90108-x

Dunin-Borkowski, R. E., McCartney, M. R., Frankel, R. B., Bazylinski, D. A., Pósfai, M., & Buseck, P. R. (1998). Magnetic microstructure of magnetotactic bacteria by electron holography. *Science*, *282*(5395), 1868–1870. https://doi.org/10.1126/science.282.5395.1868

Dunlop, D. J. (2002). Theory and application of the day plot (Mrs/Ms versus Hcr/Hc) 1. Theoretical curves and tests using titanomagnetite data. *Journal of Geophysical Research*, *107*(B3), 2056. https://doi.org/10.1029/2001jb000486

Egli, R. (2003). Analysis of the field dependence of remanent magnetization curves. *Journal of Geophysical Research*, *108*(B2), 2081. https://doi.org/10.1029/2002jb002023

Egli, R. (2004). Characterization of individual rock magnetic components by analysis of remanence curves, 1. Unmixing natural sediments. *Studia Geophysica et Geodaetica*, *48*(2), 391–446. https://doi.org/10.1023/b:sgeg.0000020839.45304.6d

Egli, R. (2013). VARIFORC: An optimized protocol for calculating non-regular first-order reversal curve (FORC) diagrams. *Global and Planetary Change*, *110*, 302–320. https://doi.org/10.1016/j.gloplacha.2013.08.003

Egli, R., Chen, A. P., Winklhofer, M., Kodama, K. P., & Horng, C.-S. (2010). Detection of noninteracting single domain particles using first-order reversal curve diagrams. *Geochemistry, Geophysics, Geosystems*, *11*(1), Q01Z11. https://doi.org/10.1029/2009gc002916

Faivre, D., & Schuler, D. (2008). Magnetotactic bacteria and magnetosomes. *Chemical Reviews*, *108*(11), 4875–4898. https://doi.org/10.1021/cr078258w

Fernández, C., & Steel, M. F. (1998). On bayesian modeling of fat tails and skewness. *Journal of the American Statistical Association*, *93*(441), 359–371. https://doi.org/10.1080/01621459.1998.10474117

Gandia, D., Gandarias, L., Marcano, L., Orue, I., Gil-Cartón, D., Alonso, J., et al. (2020). Elucidating the role of shape anisotropy in faceted magnetic nanoparticles using biogenic magnetosomes as a model. *Nanoscale*, *12*(30), 16081–16090. https://doi.org/10.1039/d0nr02189j

Ge, K., Williams, W., Liu, Q., & Yu, Y. (2014). Effects of the core-shell structure on the magnetic properties of partially oxidized magnetite grains: Experimental and micromagnetic investigations. *Geochemistry, Geophysics, Geosystems*, *15*(5), 2021–2038. https://doi.org/10.1002/2014gc005265

Geuzaine, C., & Remacle, J.-F. (2009). Gmsh: A 3-D finite element mesh generator with built-in pre-and post-processing facilities. *International Journal for Numerical Methods in Engineering*, *79*(11), 1309–1331. https://doi.org/10.1002/nme.2579

Harrison, R. J., & Lascu, I. (2014). FORCulator: A micromagnetic tool for simulating first-order reversal curve diagrams. *Geochemistry, Geophysics, Geosystems*, *15*(12), 4671–4691. https://doi.org/10.1002/2014GC005582

He, K., & Pan, Y. (2020). Magnetofossil abundance and diversity as paleoenvironmental proxies: A case study from southwest Iberian margin sediments. *Geophysical Research Letters*, *47*(8), e2020GL087165. https://doi.org/10.1029/2020gl087165

Heslop, D. (2015). Numerical strategies for magnetic mineral unmixing. *Earth-Science Reviews*, *150*, 256–284. https://doi.org/10.1016/j.earscirev.2015.07.007

Heslop, D., & Dillon, M. (2007). Unmixing magnetic remanence curves without a priori knowledge. *Geophysical Journal International*, *170*(2), 556–566. https://doi.org/10.1111/j.1365-246x.2007.03432.x

Heslop, D., Roberts, A. P., Chang, L., Davies, M., Abrajevitch, A., & De Deckker, P. (2013). Quantifying magnetite magnetofossil contributions to sedimentary magnetizations. *Earth and Planetary Science Letters*, *382*, 58–65. https://doi.org/10.1016/j.epsl.2013.09.011

Hesse, P. P. (1994). Evidence for bacterial palaeoecological origin of mineral magnetic cycles in oxic and sub-oxic Tasman Sea sediments. *Marine Geology*, *117*(1–4), 1–17. https://doi.org/10.1016/0025-3227(94)90003-5

Hovan, S. A., Rea, D. K., & Pisias, N. G. (1991). Late Pleistocene continental climate and oceanic variability recorded in northwest Pacific sediments. *Paleoceanography*, *6*(3), 349–370. https://doi.org/10.1029/91pa00559

Hu, P., Liu, Q., Torrent, J., Barrón, V., & Jin, C. (2013). Characterizing and quantifying iron oxides in Chinese loess/paleosols: Implications for pedogenesis. *Earth and Planetary Science Letters*, *369*, 271–283. https://doi.org/10.1016/j.epsl.2013.03.033

Janecek, T. R., & Rea, D. K. (1983). Eolian deposition in the northeast Pacific Ocean: Cenozoic history of atmospheric circulation. *GSA Bulletin*, *94*(6), 730–738. https://doi.org/10.1130/0016-7606(1983)94<730:EDITNP>2.0.CO;2

Joffe, I., & Heubregbr, R. (1974). Hysteresis properties of distributions of cubic single-domain ferromagnetic particles. *Philosophical Magazine*, *29*(5), 1051–1059. https://doi.org/10.1080/14786437408226590

Kirschvink, J. L., Kobayashi-Kirschvink, A., & Woodford, B. J. (1992). Magnetite biomineralization in the human brain. *Proceedings of the National Academy of Sciences*, *89*(16), 7683–7687. https://doi.org/10.1073/pnas.89.16.7683

Kling, S. A. (1982). Radiolarians from the Mariana Trough and Trench region: Deep Sea Drilling Project Leg 60. In D. Hussong, S. Uyeda, R. Knapp, H. Ellis, S. Kling, & J. Natland (Eds.), *Initial reports DSDP* (Vol. 60, pp. 537–555). US Government Printing Office. https://doi.org/10.2973/dsdp.proc.60.127.1982

Kobayashi, A., Kirschvink, J. L., Nash, C. Z., Kopp, R. E., Sauer, D. A., Bertani, L. E., & Taguchi, T. (2006). Experimental observation of magnetosome chain collapse in magnetotactic bacteria: Sedimentological, paleomagnetic, and evolutionary implications. *Earth and Planetary Science Letters*, *245*(3–4), 538–550. https://doi.org/10.1016/j.epsl.2006.03.041

Kopp, R. E., & Kirschvink, J. L. (2008). The identification and biogeochemical interpretation of fossil magnetotactic bacteria. *Earth-Science Reviews*, *86*(1–4), 42–61. https://doi.org/10.1016/j.earscirev.2007.08.001

Kopp, R. E., Weiss, B. P., Maloof, A. C., Vali, H., Nash, C. Z., & Kirschvink, J. L. (2006). Chains, clumps, and strings: Magnetofossil taphonomy with ferromagnetic resonance spectroscopy. *Earth and Planetary Science Letters*, *247*(1–2), 10–25. https://doi.org/10.1016/j.epsl.2006.05.001

Kumagai, Y., Nakamura, N., Sato, T., Oka, T., & Oda, H. (2018). Ferromagnetic resonance spectroscopy and rock magnetic characterization of fossil coral skeletons in Ishigaki islands, Japan. *Geosciences*, *8*(11), 400. https://doi.org/10.3390/geosciences8110400

Lascu, I., & Plank, C. (2013). A new dimension to sediment magnetism: Charting the spatial variability of magnetic properties across lake basins. *Global and Planetary Change*, *110*, 340–349. https://doi.org/10.1016/j.gloplacha.2013.03.013

Lean, C. M. B., & McCave, I. N. (1998). Glacial to interglacial mineral magnetic and palaeoceanographic changes at Chatham rise, SW Pacific Ocean. *Earth and Planetary Science Letters*, *163*(1–4), 247–260. https://doi.org/10.1016/s0012-821x(98)00191-5

Lefèvre, C. T., Abreu, F., Schmidt, M. L., Lins, U., Frankel, R. B., Hedlund, B. P., & Bazylinski, D. A. (2010). Moderately thermophilic magnetotactic bacteria from hot springs in Nevada. *Applied and Environmental Microbiology*, *76*(11), 3740–3743. https://doi.org/10.1128/aem.03018-09

Lefèvre, C. T., & Bazylinski, D. A. (2013). Ecology, diversity, and evolution of magnetotactic bacteria. *Microbiology and Molecular Biology Reviews*, *77*(3), 497–526. https://doi.org/10.1128/mmbr.00021-13

Lefèvre, C. T., Frankel, R. B., Pósfai, M., Prozorov, T., & Bazylinski, D. A. (2011). Isolation of obligately alkaliphilic magnetotactic bacteria from extremely alkaline environments. *Environmental Microbiology*, *13*(8), 2342–2350. https://doi.org/10.1111/j.1462-2920.2011.02505.x

Li, J., Liu, Y., Liu, S., Roberts, A. P., Pan, H., Xiao, T., & Pan, Y. (2020). Classification of a complexly mixed magnetic mineral assemblage in Pacific Ocean surface sediment by electron microscopy and supervised magnetic unmixing. *Frontiers of Earth Science*, *8*, 609058. https://doi.org/10.3389/feart.2020.609058

Li, J., Menguy, N., Leroy, E., Roberts, A. P., Liu, P., & Pan, Y. (2020). Biomineralization and magnetism of uncultured magnetotactic coccus strain THC-1 with non-chained magnetosomal magnetite nanoparticles. *Journal of Geophysical Research: Solid Earth*, *125*(12), e2020JB020853. https://doi.org/10.1029/2020JB020853

Li, J., & Pan, Y. (2012). Environmental factors affect magnetite magnetosome synthesis in magnetospirillum magneticum AMB-1: Implications for biologically controlled mineralization. *Geomicrobiology Journal*, *29*(4), 362–373. https://doi.org/10.1080/01490451.2011.565401

Li, J., Wu, W., Liu, Q., & Pan, Y. (2012). Magnetic anisotropy, magnetostatic interactions and identification of magnetofossils. *Geochemistry, Geophysics, Geosystems*, *13*(10), Q10Z51. https://doi.org/10.1029/2012GC004384

Liu, P., Liu, Y., Zhao, X., Roberts, A. P., Zhang, H., Zheng, Y., & Li, J. (2021). Diverse phylogeny and morphology of magnetite biomineralized by magnetotactic cocci. *Environmental Microbiology*, 1462–2920. https://doi.org/10.1111/1462-2920.15254

Maxbauer, D. P., Feinberg, J. M., & Fox, D. L. (2016). MAX UnMix: A web application for unmixing magnetic coercivity distributions. *Computers and Geosciences*, *95*, 140–145. https://doi.org/10.1016/j.cageo.2016.07.009

McKay, D. S., Gibson, E. K., Thomas-Keprta, K. L., Vali, H., Romanek, C. S., Clemett, S. J., et al. (1996). Search for past life on Mars: Possible relic biogenic activity in Martian meteorite ALH84001. *Science*, *273*(5277), 924–930. https://doi.org/10.1126/science.273.5277.924

Moskowitz, B. M., Frankel, R. B., & Bazylinski, D. A. (1993). Rock magnetic criteria for the detection of biogenic magnetite. *Earth and Planetary Science Letters*, *120*(3–4), 283–300. https://doi.org/10.1016/0012-821x(93)90245-5

Moskowitz, B. M., Frankel, R. B., Walton, S. A., Dickson, D. P. E., Wong, K. K. W., Douglas, T., & Mann, S. (1997). Determination of the pre-exponential frequency factor for superparamagnetic maghemite particles in magnetoferritin. *Journal of Geophysical Research*, *102*(B10), 22671–22680. https://doi.org/10.1029/97jb01698

Muxworthy, A. R., & Williams, W. (2009). Critical superparamagnetic/single-domain grain sizes in interacting magnetite particles: Implications for magnetosome crystals. *Journal of The Royal Society Interface*, *6*(41), 1207–1212. https://doi.org/10.1098/rsif.2008.0462

Olszewska-Widdrat, A., Schiro, G., Reichel, V. E., & Faivre, D. (2019). Reducing conditions favor magnetosome production in Magnetospirillum magneticum AMB-1. *Frontiers in Microbiology*, *10*, 582. https://doi.org/10.3389/fmicb.2019.00582

Ouyang, T., Heslop, D., Roberts, A. P., Tian, C., Zhu, Z., Qiu, Y., & Peng, X. (2014). Variable remanence acquisition efficiency in sediments containing biogenic and detrital magnetites: Implications for relative paleointensity signal recording. *Geochemistry, Geophysics, Geosystems*, *15*(7), 2780–2796. https://doi.org/10.1002/2014gc005301

Paterson, G. A., Zhao, X., Jackson, M., & Heslop, D. (2018). Measuring, processing, and analyzing hysteresis data. *Geochemistry, Geophysics, Geosystems*, *19*(7), 1925–1945. https://doi.org/10.1029/2018gc007620

Petersen, N., von Dobeneck, T., & Vali, H. (1986). Fossil bacterial magnetite in deep-sea sediments from the South Atlantic Ocean. *Nature*, *320*(6063), 611–615. https://doi.org/10.1038/320611a0

Pike, C. R., Roberts, A. P., & Verosub, K. L. (1999). Characterizing interactions in fine magnetic particle systems using first order reversal curves. *Journal of Applied Physics*, *85*(9), 6660–6667. https://doi.org/10.1063/1.370176

Rea, D. K. (1994). The paleoclimatic record provided by eolian deposition in the deep sea: The geologic history of wind. *Reviews of Geophysics*, *32*(2), 159. https://doi.org/10.1029/93RG03257

Rea, D. K., Snoeckx, H., & Joseph, L. H. (1998). Late Cenozoic eolian deposition in the North Pacific: Asian drying, Tibetan uplift, and cooling of the northern hemisphere. *Paleoceanography*, *13*(3), 215–224. https://doi.org/10.1029/98pa00123

Roberts, A. P., Almeida, T. P., Church, N. S., Harrison, R. J., Heslop, D., Li, Y., et al. (2017). Resolving the origin of pseudo-single domain magnetic behavior. *Journal of Geophysical Research: Solid Earth*, *122*(12), 9534–9558. https://doi.org/10.1002/2017jb014860

Roberts, A. P., Florindo, F., Chang, L., Heslop, D., Jovane, L., & Larrasoana, J. C. (2013). Magnetic properties of pelagic marine carbonates. *Earth-Science Reviews*, *127*, 111–139. https://doi.org/10.1016/j.earscirev.2013.09.009

Roberts, A. P., Pike, C. R., & Verosub, K. L. (2000). First-order reversal curve diagrams: A new tool for characterizing the magnetic properties of natural samples. *Journal of Geophysical Research*, *105*(B12), 28461–28475. https://doi.org/10.1029/2000jb900326

Shimono, T., & Yamazaki, T. (2016). Environmental rock-magnetism of Cenozoic red clay in the South Pacific gyre. *Geochemistry, Geophysics, Geosystems*, *17*(4), 1296–1311. https://doi.org/10.1002/2015GC006062

Shipboard Engineering and Scientific Parties. (1990). Site 777. In B. W. Harding, M. A. Storms, et al. (Eds.), *Proceedings of the Ocean Drilling Program, 124E Initial Reports* (pp. 111–135). Ocean Drilling Program. https://doi.org/10.2973/odp.proc.ir.124e.118.1990

Smirnov, A. V., & Tarduno, J. A. (2000). Low-temperature magnetic properties of pelagic sediments (Ocean Drilling Program Site 805C): Tracers of maghemitization and magnetic mineral reduction. *Journal of Geophysical Research*, *105*(B7), 16457–16471. https://doi.org/10.1029/2000jb900140

Solov'yov, I. A., & Greiner, W. (2009). Micromagnetic insight into a magnetoreceptor in birds: Existence of magnetic field amplifiers in the beak. *Physical Review E*, *80*(4), 41919. https://link.aps.org/doi/10.1103/PhysRevE.80.041919

Tanaka, E., Nakamura, K., Yasukawa, K., Mimura, K., Fujinaga, K., Ohta, J., et al. (2020). Chemostratigraphic correlations of deep-sea sediments in the western North Pacific Ocean: A new constraint on the distribution of mud highly enriched in rare-earth elements. *Minerals*, *10*(6), 575. https://doi.org/10.3390/min10060575

Thomas-Keprta, K. L., Bazylinski, D. A., Kirschvink, J. L., Clemett, S. J., McKay, D. S., Wentworth, S. J., et al. (2000). Elongated prismatic magnetite crystals in ALH84001 carbonate globules: Potential martian magnetofossils. *Geochimica et Cosmochimica Acta*, *64*(23), 4049–4081. https://doi.org/10.1016/s0016-7037(00)00481-6

Thomas-Keprta, K. L., Clemett, S. J., Bazylinski, D. A., Kirschvink, J. L., McKay, D. S., Wentworth, S. J., et al. (2001). Truncated hexa-octahedral magnetite crystals in ALH84001: Presumptive biosignatures. *Proceedings of the National Academy of Sciences*, *98*(5), 2164–2169. https://doi.org/10.1073/pnas.051500898

Torii, M. (1997). Low-temperature oxidation and subsequent downcore dissolution of magnetite in deep-sea sediments, ODP Leg 161 (Western Mediterranean). *Journal of Geomagnetism and Geoelectricity*, *49*(10), 1233–1245. https://doi.org/10.5636/jgg.49.1233

Uebe, R., & Schüler, D. (2016). Magnetosome biogenesis in magnetotactic bacteria. *Nature Reviews Microbiology*, *14*(10), 621–637. https://doi.org/10.1038/nrmicro.2016.99

Usui, Y., Shimono, T., & Yamazaki, T. (2018). Rock magnetism of quartz and feldspars chemically separated from pelagic red clay: A new approach to provenance study. *Earth Planets and Space*, *70*(1), 153. https://doi.org/10.1186/s40623-018-0918-1

Usui, Y., & Yamazaki, T. (2021). Magnetostratigraphic evidence for post-depositional distortion of osmium isotopic records in pelagic clay and its implications for mineral flux estimates. *Earth Planets and Space*, *73*(1), 2. https://doi.org/10.1186/s40623-020-01338-4

Usui, Y., Yamazaki, T., Oka, T., & Kumagai, Y. (2019). Inverse magnetic susceptibility fabrics in pelagic sediment: Implications for magnetofossil abundance and alignment. *Journal of Geophysical Research: Solid Earth*, *124*(11), 10672–10686. https://doi.org/10.1029/2019JB018128

Usui, Y., Yamazaki, T., & Saitoh, M. (2017). Changing abundance of magnetofossil morphologies in pelagic red clay around minamitorishima, western North Pacific. *Geochemistry, Geophysics, Geosystems*, *18*(12), 4558–4572. https://doi.org/10.1002/2017GC007127

Vali, H., & Kirschvink, J. L. (1989). Magnetofossil dissolution in a palaeomagnetically unstable deep-sea sediment. *Nature*, *339*(6221), 203–206. https://doi.org/10.1038/339203a0

Von Dobeneck, T., Petersen, N., & Vali, H. (1987). Bakterielle magnetofossilien. *Geowissenschaften in Unserer Zeit*, *5*, 27–35.

Weiss, B. P., Kim, S. S., Kirschvink, J. L., Kopp, R. E., Sankaran, M., Kobayashi, A., & Komeili, A. (2004a). Ferromagnetic resonance and low-temperature magnetic tests for biogenic magnetite. *Earth and Planetary Science Letters*, *224*(1–2), 73–89. https://doi.org/10.1016/j.epsl.2004.04.024

Weiss, B. P., Kim, S. S., Kirschvink, J. L., Kopp, R. E., Sankaran, M., Kobayashi, A., & Komeili, A. (2004b). Magnetic tests for magnetosome chains in Martian meteorite ALH84001. *Proceedings of the National Academy of Sciences*, *101*(22), 8281–8284. https://doi.org/10.1073/pnas.0402292101

Wessel, P., Luis, J., Uieda, L., Scharroo, R., Wobbe, F., Smith, W., & Tian, D. (2019). The Generic Mapping Tools Version 6. *Geochemistry, Geophysics, Geosystems*, *20*(11), 5556–5564. https://doi.org/10.1029/2019gc008515

Yamazaki, T. (2008). Magnetostatic interactions in deep-sea sediments inferred from first-order reversal curve diagrams: Implications for relative paleointensity normalization. *Geochemistry, Geophysics, Geosystems*, *9*(2), Q02005. https://doi.org/10.1029/2007GC001797

Yamazaki, T. (2009). Environmental magnetism of Pleistocene sediments in the North Pacific and Ontong-Java plateau: Temporal variations of detrital and biogenic components. *Geochemistry, Geophysics, Geosystems*, *10*(7), Q07Z04. https://doi.org/10.1029/2009gc002413

Yamazaki, T. (2012). Paleoposition of the intertropical convergence zone in the eastern Pacific inferred from glacial-interglacial changes in terrigenous and biogenic magnetic mineral fractions. *Geology*, *40*(2), 151–154. https://doi.org/10.1130/g32646.1

Yamazaki, T., Fu, W., Shimono, T., & Usui, Y. (2020). Unmixing biogenic and terrigenous magnetic mineral components in red clay of the Pacific Ocean using principal component analyses of first-order reversal curve diagrams and paleoenvironmental implications. *Earth Planets and Space*, *72*(1), 120. https://doi.org/10.1186/s40623-020-01248-5

Yamazaki, T., & Ikehara, M. (2012). Origin of magnetic mineral concentration variation in the Southern Ocean. *Paleoceanography*, *27*(2), PA2206. https://doi.org/10.1029/2011PA002271

Yamazaki, T., & Ioka, N. (1997). Environmental rock-magnetism of pelagic clay: Implications for Asian eolian input to the North Pacific since the Pliocene. *Paleoceanography*, *12*(1), 111–124. https://doi.org/10.1029/96pa02757

Yamazaki, T., & Kawahata, H. (1998). Organic carbon flux controls the morphology of magnetofossils in marine sediments. *Geology*, *26*(12), 1064–1066. https://doi.org/10.1130/0091-7613(1998)026<1064:ocfctm>2.3.co;2

Yamazaki, T., & Shimono, T. (2013). Abundant bacterial magnetite occurrence in oxic red clay. *Geology*, *41*(11), 1191–1194. https://doi.org/10.1130/G34782.1

Yamazaki, T., Suzuki, Y., Kouduka, M., & Kawamura, N. (2019). Dependence of bacterial magnetosome morphology on chemical conditions in deep-sea sediments. *Earth and Planetary Science Letters*, *513*, 135–143. https://doi.org/10.1016/j.epsl.2019.02.015

Yamazaki, T., Yamamoto, Y., Acton, G., Guidry, E. P., & Richter, C. (2013). Rock-magnetic artifacts on long-term relative paleointensity variations in sediments. *Geochemistry, Geophysics, Geosystems*, *14*(1), 29–43. https://doi.org/10.1002/ggge.20064

Zhang, Q., & Liu, Q. (2018). Changes in diffuse reflectance spectroscopy properties of hematite in sediments from the North Pacific Ocean and implications for eolian dust evolution history. *Earth and Planetary Physics*, *2*(4), 342–350. https://doi.org/10.26464/epp2018031

Zhang, Q., Liu, Q., Li, J., & Sun, Y. (2018). An integrated study of the eolian dust in pelagic sediments from the North Pacific Ocean based on environmental magnetism, transmission electron microscopy, and diffuse reflectance spectroscopy. *Journal of Geophysical Research: Solid Earth*, *123*(5), 3358–3376. https://doi.org/10.1002/2017JB014951

Zhang, Q., Liu, Q., Roberts, A. P., Larrasoaña, J. C., Shi, X., & Jin, C. (2020). Mechanism for enhanced eolian dust flux recorded in North Pacific Ocean sediments since 4.0 Ma: Aridity or humidity at dust source areas in the Asian interior? *Geology*, *48*(1), 77–81. https://doi.org/10.1130/g46862.1